Electric dipole polarizability from first principles calculations

M. Miorelli, S. Bacca, N. Barnea, G. Hagen, G. R. Jansen, G. Orlandini, and T. Papenbrock

Phys. Rev. C **94**, 034317 — Published 19 September 2016

DOI: 10.1103/PhysRevC.94.034317

Electric dipole polarizability from first principles calculations

M. Miorelli,[1,2] S. Bacca,[1,3] N. Barnea,[4] G. Hagen,[5,6] G. R. Jansen,[5,7] G. Orlandini,[8,9] and T. Papenbrock[5,6]

[1] *TRIUMF, 4004 Wesbrook Mall, Vancouver, BC, V6T 2A3, Canada*
[2] *Department of Physics and Astronomy, University of British Columbia, Vancouver, BC, V6T 1Z4, Canada*
[3] *Department of Physics and Astronomy, University of Manitoba, Winnipeg, MB, R3T 2N2, Canada*
[4] *Racah Institute of Physics, Hebrew University, 91904, Jerusalem*
[5] *Physics Division, Oak Ridge National Laboratory, Oak Ridge, TN 37831, USA*
[6] *Department of Physics and Astronomy, University of Tennessee, Knoxville, TN 37996, USA*
[7] *National Center for Computational Sciences, Oak Ridge National Laboratory, Oak Ridge, TN 37831 USA*
[8] *Dipartimento di Fisica, Università di Trento, Via Sommarive 14, I-38123 Trento, Italy*
[9] *Istituto Nazionale di Fisica Nucleare, TIFPA, Via Sommarive 14, I-38123 Trento, Italy*

(Dated: August 19, 2016)

The electric dipole polarizability quantifies the low-energy behavior of the dipole strength and is related to critical observables such as the radii of the proton and neutron distributions. Its computation is challenging because most of the dipole strength lies in the scattering continuum. In this paper we combine integral transforms with the coupled-cluster method and compute the dipole polarizability using bound-state techniques. Employing different interactions from chiral effective field theory, we confirm the strong correlation between the dipole polarizability and the charge radius, and study its dependence on three-nucleon forces. We find good agreement with data for the ^{4}He, ^{40}Ca, and ^{16}O nuclei, and predict the dipole polarizability for the rare nucleus ^{22}O.

PACS numbers: 21.60.De, 24.10.Cn, 24.30.Cz, 25.20.-x

I. INTRODUCTION

The electric dipole polarizability α_D in nuclei has been subject of intense studies, both from the experimental and the theoretical side. Photo-absorption studies have focused on the determination of the giant dipole resonances (GDR) in stable nuclei, originally interpreted as a collective motion of all protons oscillating against all neutrons [1]. The discovery of a soft peak at low energies in neutron-rich and unstable nuclei, i.e. the pygmy dipole resonance (PDR), has spurred a renewed interest in the electric dipole response [2]. For a recent review, we refer the reader to Ref. [3].

Calculations based on relativistic and non-relativistic density-functional theory pointed out that α_D is very strongly correlated with the neutron-skin thickness [4–6]. This can be contrasted to *ab initio* computations based on Hamiltonians from chiral effective field theory (EFT) that rather found a strong correlation between the charge and the neutron radii with α_D in ^{48}Ca [7]. In any case, the dipole polarizability is sensitive to the neutron distribution, and thereby constrains the neutron equation of state and the physics of neutron stars [8–11]. The equation of state of asymmetric nuclear matter depends on a few parameters, such as the slope of the symmetry energy, which correlates with GDR [12] and PDR [13] features.

Recent experiments measured the dipole polarizability in ^{208}Pb [14], ^{68}Ni [15], and ^{120}Sn [16, 17], and data for ^{48}Ca is presently being analyzed by the Darmstadt-Osaka collaboration. Only scarce data exist on unstable nuclei, but recent activity was devoted, *e.g.*, to ^{22,24}O [18].

The dipole polarizability

$$\alpha_D = 2\alpha \int_{\omega_{ex}}^{\infty} d\omega \, \frac{R(\omega)}{\omega} \,, \tag{1}$$

where α is the fine structure constant, is an inverse energy weighted sum rule of the dipole response function $R(\omega)$. Thus, the determination of the low-energy dipole strength is crucial. Here ω is the excitation energy and ω_{ex} is the energy of the first state excited by the dipole referred to the ground-state. Within one isotopic chain one expects that neutron-rich nuclei with a significant low-lying dipole strength also exhibit a larger polarizability than other isotopes. To both interpret recent data and guide new experiments, it is important to theoretically map the evolution of α_D as a function of neutron number. Theories that can reliably address exotic nuclei far from the valley of stability are needed and *ab initio* methods are best positioned to deliver both predictive power [19–21] and estimates of the theoretical uncertainties [22–25].

This paper is organized as follows. Section II describes the theoretical approach based on integral transforms and the coupled-cluster method. In Section III

we present results for the nuclei ^{4}He, ^{16,22}O and ^{40}Ca. First, we compare different computational approaches with each other. Second, we present results for the dipole polarizability in these nuclei based on an interaction from chiral EFT that exhibits accurate saturation properties [26]. Third, we study correlations between the dipole polarizability and charge radii based on a variety of nucleon-nucleon (NN) interactions and interactions that also include three-nucleon forces (3NFs). Finally, we summarize our results in Sect. IV.

II. THEORETICAL APPROACH

The electric dipole polarizability in Eq. (1) depends on the dipole response function

$$R(\omega) = \sum\!\!\!\!\!\!\int_f \langle\Psi_0|\hat{\Theta}^\dagger|\Psi_f\rangle\langle\Psi_f|\hat{\Theta}|\Psi_0\rangle\delta(E_f - E_0 - \omega). \quad (2)$$

Here $\hat{\Theta} = \sum_{i=1}^{A} P_i(z_i - Z_{cm})$ is the dipole excitation operator, where P_i is the proton projection operator and z_i/Z_{cm} the nucleon/center of mass z-coordinate, respectively. $|\Psi_0\rangle$ is the ground-state of the nucleus and $|\Psi_f\rangle$ represents the excited states. The latter can be both in the discrete and in the continuum region of spectrum, and this is reflected by the combined discrete and continuum symbol $\sum\!\!\!\!\!\!\int_f$ [27]. From Eqs. (1) and (2) it is clear that the dipole polarizability contains the information on $R(\omega)$ at all energies ω, including those in the continuum. A calculation of α_D would then require to be able to solve the many-body scattering problem at such energies, which is extremely difficult for nuclei with mass number larger than four.

To make progress, we rewrite α_D as a sum rule of the response function. Starting from Eq. (1) and using the completeness of the Hamiltonian eigenstates $\mathbb{I} = \sum\!\!\!\!\!\!\int_f |\Psi_f\rangle\langle\Psi_f|$ we obtain

$$\alpha_D = \langle\Psi_0|\hat{\Theta}^\dagger \frac{1}{\hat{H} - E_0}\hat{\Theta}|\Psi_0\rangle\,. \quad (3)$$

One way to calculate α_D by means of the sum rule in Eq. (3) is to represent the Hamiltonian on a finite basis of N basis functions $|n\rangle$. After diagonalization of the Hamiltonian matrix $H_{n,n'}$, one obtains its N eigenstates $|\beta\rangle$ and eigenvalues E_β, and Eq. (3) becomes

$$\alpha_D = \sum_{\beta}^{N} \langle\Psi_0|\hat{\Theta}^\dagger|\beta\rangle\langle\beta|\frac{1}{E_\beta - E_0}|\beta\rangle\langle\beta|\hat{\Theta}|\Psi_0\rangle\,. \quad (4)$$

Increasing N yields an increasingly more accurate representation of the eigenfunctions $|\beta\rangle$ and eigenvalues E_β of $\hat{H}$, and eventually the value of α_D would converge. In practical cases, however, the truncated basis states $|n\rangle$ used to represent the Hamiltonian are discrete and have a finite norm. Because the spectrum of $\hat{H}$ has both a discrete and a continuum part, one may question the use of such a discrete basis. Similarly to Ref. [28], we will show that this approach is rigorous and works quite well also within coupled-cluster theory.

A. Integral transforms

Integral transforms reduce the continuum problem of calculating $R(\omega)$ to the solution of a bound-state-like problem [29–31]. In such an approach, one first calculates the integral transform $\mathcal{I}(\sigma)$ of the response function. In a second step, one might invert the integral transform to obtain the response function $R(\omega)$, or one might compute relevant observables (such as the dipole polarizability) directly from the integral transform. Here, we will use the Stieltjes integral transform [32] for the direct computation of the dipole polarizability.

The Stieltjes integral transform reads

$$\mathcal{I}(\sigma) = \int \frac{R(\omega)}{\omega + \sigma} d\omega, \quad (5)$$

with σ real and positive. Using the completeness on the Hamiltonian eigenstates and the definition of the response function from Eq. (2) yields

$$\begin{aligned}\mathcal{I}(\sigma) &= \langle\Psi_0|\hat{\Theta}^\dagger \frac{1}{\hat{H} - E_0 + \sigma}\hat{\Theta}|\Psi_0\rangle \\ &= \langle\Psi_0|\hat{\Theta}^\dagger|\tilde{\Psi}(\sigma)\rangle,\end{aligned} \quad (6)$$

where we have defined

$$|\tilde{\Psi}(\sigma)\rangle \equiv \frac{1}{\hat{H} - E_0 + \sigma}\hat{\Theta}|\Psi_0\rangle. \quad (7)$$

The function $|\tilde{\Psi}(\sigma)\rangle$ is the solution of the following Schrödinger-like equation with a source

$$(\hat{H} - E_0 + \sigma)|\tilde{\Psi}(\sigma)\rangle = \hat{\Theta}|\Psi_0\rangle. \quad (8)$$

Since $\sigma > 0$, and for large inter particle distances $|\Psi_0\rangle \to 0$, one has that asymptotically – and for non singular operators $\hat{\Theta}$ – $|\tilde{\Psi}(\sigma)\rangle$ should satisfy a Schrödinger equation with eigenvalues smaller than E_0. This implies that $|\tilde{\Psi}(\sigma)\rangle \to 0$ asymptotically, namely it has bound state-like asymptotic conditions. We are therefore allowed to calculate $\mathcal{I}(\sigma)$ using a bound-state basis expansion, *i.e.* an L_2 square integrable basis such as harmonic oscillator functions. Noticing that Eq. (6) differs from Eq. (3) only by the presence of $\sigma > 0$, we proceed as it was described above, namely using a representation on a bound state basis and increasing the number N of basis functions up to convergence. Then the value of α_D can be obtained as

$$\alpha_D = 2\alpha \lim_{\sigma\to 0^+} \mathcal{I}(\sigma)\,, \quad (9)$$

avoiding the continuum problem. The limit taken with positive σ is crucial not only to allow the use of a bound

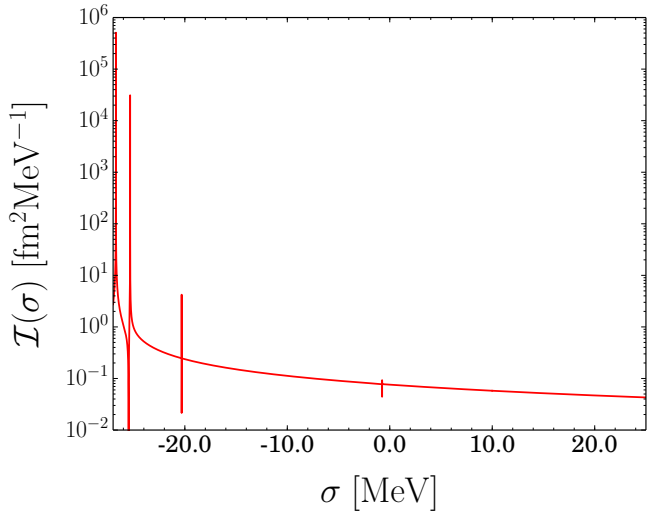

FIG. 1. (Color online) The Stieltjes integral transform $\mathcal{I}(\sigma)$ as a function of σ in the case of ^{4}He.

state basis, but also because it avoids poles (we recall that E_0 is negative). For $\sigma < 0$ poles will certainly be present, presumably at different places depending on the basis. We indeed observe several poles in the region of $\sigma < 0$, while the curve is persistently smooth for $\sigma \geq 0$ in Fig. 1, where we show $\mathcal{I}(\sigma)$ for ^{4}He calculated with a realistic interaction [26], as detailed later. We choose ^{4}He, where calculations are faster and can be benchmarked with few-body methods.

Below we will use an implementation of Eq. (9) to compute the dipole polarizability of heavier nuclei. To test this approach, we will also compare it to α_D obtained by the dipole response function as in Eq. (1). If one were able to invert the Stieltjes transform, one could obtain $R(\omega)$ to calculate the integral in Eq. (1). Unfortunately, the inversion of this integral transform presents the typical difficulties of an ill-posed problem. In fact in Ref. [32] it was shown that inversions performed with the regularization method [33] generate quite different responses, all compatible with the same Stieltjes transform within numerical errors. Therefore, we will employ the much more suitable Lorentz integral transform (LIT) [30, 31]

$$L(\sigma,\Gamma) = \frac{\Gamma}{\pi}\int \frac{R(\omega)}{(\omega-\sigma)^2+\Gamma^2}d\omega, \qquad (10)$$

where $\Gamma, \sigma \in \mathbb{R}$ and $\Gamma > 0$. The Lorentzian kernel $L(\sigma,\Gamma)$ is peaked at σ and has the width Γ. The LIT can be much more easily inverted to yield the response function, because the width Γ introduces a finite resolution. Thus, the response function is smeared only in a narrow region of space determined by the width Γ.

The calculation the Lorentz transform proceeds as for the Stieltjes transform, using the definition of response function and the completeness of the eigenfunctions of the Hamiltonian. One finds

$$L(z) = \frac{\Gamma}{\pi}\langle\Psi_0|\hat{\Theta}^\dagger \frac{1}{(\hat{H}-z^*)}\frac{1}{(\hat{H}-z)}\hat{\Theta}|\Psi_0\rangle, \qquad (11)$$

with $z = E_0 + \sigma + i\Gamma$. The LIT can be rewritten in a form that resembles Eq. (6) as

$$\begin{aligned} L(z) &= \frac{1}{\pi}\mathfrak{Im}\left[\langle\Psi_0|\hat{\Theta}^\dagger\frac{1}{(\hat{H}-z)}\hat{\Theta}|\Psi_0\rangle\right] \\ &= \frac{1}{\pi}\mathfrak{Im}\left[\langle\Psi_0|\hat{\Theta}^\dagger|\tilde{\Psi}(z)\rangle\right]. \end{aligned} \qquad (12)$$

Here we defined the function

$$|\tilde{\Psi}(z)\rangle \equiv \frac{1}{\hat{H}-z}\hat{\Theta}|\Psi_0\rangle. \qquad (13)$$

Similarly as for Eq. (7), $|\tilde{\Psi}(z)\rangle$ has a bound-state-like nature and a finite norm

$$\langle\tilde{\Psi}(z)|\tilde{\Psi}(z)\rangle = L(z) = \frac{\Gamma}{\pi}\int\frac{R(\omega)}{(\omega-\sigma)^2+\Gamma^2}d\omega < \infty. \qquad (14)$$

A couple of remarks are in order here. First, we note that the positive parameter σ enters in the Stieltjes and Lorentz transforms with a minus and a plus sign respectively. While in the Stieltjes transform the bound-state-like nature of $|\tilde{\Psi}\rangle$ is due to that minus sign, in the Lorentz case it is due to the presence of the imaginary part Γ. Second, in the limit $\Gamma \to 0$ the Lorentzian kernel becomes a delta function

$$L(\sigma,\Gamma\to 0) = \int R(\omega)\delta(\omega-\sigma)d\omega = R(\sigma). \qquad (15)$$

This allows us to estimate the dipole polarizability also using Eq. (15) together with Eq. (1)

$$\alpha_D = 2\alpha\int\frac{L(\sigma,\Gamma\to 0)}{\sigma}d\sigma. \qquad (16)$$

However, in L(σ,Γ) one must be careful in taking smaller and smaller Γ since the convergence in the model space expansion becomes increasingly difficult.

B. Coupled-cluster implementation

In this Subsection we will compute the dipole polarizability via Eq. (9) with the coupled-cluster method. This calculation proceeds similarly as done for the LIT in Refs. [34, 35].

Coupled-cluster theory [36–43] is based on the exponential ansatz for the ground-state

$$|\Psi_0\rangle = e^{\hat{T}}|0_R\rangle, \qquad (17)$$

see Refs. [44, 45] for recent reviews. Here, $|0_R\rangle$ is a reference product state, and the cluster operator T introduces particle-hole (p-h) excitations into the reference. Using

second quantization, and normal ordering the dipole excitation operator with respect to the reference state yields the response function [35]

$$R(\omega) = \sum_n \langle 0_L|\overline{\Theta}^\dagger|n_R\rangle\langle n_L|\overline{\Theta}|0_R\rangle\delta(\Delta E_n - \Delta E_0 - \omega). \quad (18)$$

Here ΔE_n, ΔE_0 are the correlation energies of the nth-excited state and ground-state respectively, and solve

$$\begin{aligned} \overline{H}|0_R\rangle &= \Delta E_0|0_R\rangle \quad \text{or} \quad \langle 0_L|\overline{H} = \langle 0_L|\Delta E_0, \\ \overline{H}|n_R\rangle &= \Delta E_n|n_R\rangle \quad \text{or} \quad \langle n_L|\overline{H} = \langle n_L|\Delta E_n. \end{aligned} \quad (19)$$

Here we used similarity-transformed operators via

$$\overline{O} = e^{-\hat{T}}\hat{O}_N e^{+\hat{T}}, \quad (20)$$

and $\hat{O}_N$ is the normal-ordered form of any operator $\hat{O}$, *e.g.* $\hat{H}$ or $\hat{\Theta}$. Substituting Eq. (18) in Eq. (5), and making use of the expressions in Eq. (19) yields

$$\mathcal{I}(\sigma) = \langle 0_L|\overline{\Theta}^\dagger \frac{1}{\overline{H} - \Delta E_0 + \sigma}\overline{\Theta}|0_R\rangle. \quad (21)$$

This equation resembles Eq. (6), when operators are replaced by their similarity transformed counterparts, and one needs to distinguish between left and right states because of the non-Hermitian nature of the excitation operator $\hat{T}$. We proceed as in Subsection II A, and define a state $|\tilde{\Psi}(\sigma)\rangle$ as the solution of

$$(\overline{H} - \Delta E_0 + \sigma)|\tilde{\Psi}_R(\sigma)\rangle = \overline{\Theta}|0_R\rangle. \quad (22)$$

Eq. (22) resembles Eq. (15) in [35] and can be solved using the equation-of-motion coupled-cluster method for excited states [46]. In this approach, one regards

$$\begin{aligned} |\tilde{\Psi}_R(\sigma)\rangle =& \hat{\mathcal{R}}(\sigma)|0_R\rangle \equiv \left(r_0(\sigma) + \sum_{i,a} r_i^a(\sigma)\hat{c}_a^\dagger\hat{c}_i + \right. \\ &\left. + \frac{1}{4}\sum_{i,j,a,b} r_{ij}^{ab}(\sigma)\hat{c}_a^\dagger\hat{c}_b^\dagger\hat{c}_j\hat{c}_i + \ldots \right)|0_R\rangle \\ \equiv& \sum_\alpha \hat{C}_\alpha r_\alpha(\sigma)|0_R\rangle \equiv \hat{\mathbf{C}}\cdot\mathbf{r}(\sigma)|0_R\rangle, \end{aligned} \quad (23)$$

as an excited state of the similarity-transformed Hamiltonian $\overline{H}$ based on p-h excitations of the reference. In the last line of Eq. (23) the index α labels the 0p-0h, 1p-1h, 2p-2h, ... states

$$|\Phi_\alpha\rangle \equiv |0_R\rangle, |\Phi_i^a\rangle, |\Phi_{ij}^{ab}\rangle, \ldots. \quad (24)$$

We also defined the column vector $\mathbf{r}(\sigma)$ with elements $r_0(\sigma), r_i^a(\sigma), r_{ij}^{ab}(\sigma), \ldots$ and a row vector $\hat{\mathbf{C}}$ whose elements are strings of normal-ordered creation and annihilation operators. Combining Eq. (22) with Eq. (19) and the linear ansatz for $|\tilde{\Psi}(\sigma)\rangle$, the Stieltjes transform becomes

$$\mathcal{I}(\sigma) = \langle 0_L|\overline{\Theta}^\dagger\hat{\mathcal{R}}(\sigma)|0_R\rangle = \mathbf{S}^L\mathbf{M}(\sigma)^{-1}\mathbf{S}^R. \quad (25)$$

Here $\mathbf{S}^L$ and $\mathbf{S}^R$ are row- and column-vectors respectively with elements

$$\begin{aligned} S_\alpha^R &= \langle\Phi_\alpha|\overline{\Theta}|0_R\rangle, \\ S_\alpha^L &= \langle 0_L|\overline{\Theta}^\dagger|\Phi_\alpha\rangle, \end{aligned} \quad (26)$$

and $\mathbf{M}$ is a matrix with elements

$$M_{\alpha\beta}(\sigma) = \langle\Phi_\alpha|\left[\overline{H}, \hat{C}_\beta\right]|0_R\rangle + \sigma\delta_{\alpha\beta}. \quad (27)$$

The right-hand side of Eq. (25) can be calculated using the Lanczos procedure. Because we are dealing with non-Hermitian operators, we have to make use of the generalized Lanczos algorithm for non-symmetric matrices [47]. In this approach, one first defines two pivot vectors

$$\begin{aligned} \mathbf{v}_0 &= \frac{\mathbf{S}^R}{\sqrt{\mathbf{S}^L\cdot\mathbf{S}^R}}, \\ \mathbf{w}_0 &= \frac{\mathbf{S}^L}{\sqrt{\mathbf{S}^L\cdot\mathbf{S}^R}}, \end{aligned} \quad (28)$$

and repeated application of the matrix $\mathbf{M}(\sigma)$ generates the Lanczos basis in which $\mathbf{M}$ is tri-diagonal

$$\mathbf{M}(\sigma) = \begin{pmatrix} a_0-\sigma & b_0 & 0 & 0 & \cdots \\ b_0 & a_1-\sigma & b_1 & 0 & \cdots \\ 0 & b_1 & a_2-\sigma & b_2 & \cdots \\ 0 & 0 & b_2 & a_3-\sigma & \cdots \\ \vdots & \vdots & \vdots & \vdots & \ddots \end{pmatrix}. \quad (29)$$

In what follows, we employ the matrix $\mathbf{M}$ in the Lanczos basis. We note that $\mathbf{S}^L\cdot\mathbf{S}^R = \langle 0_L|\overline{\Theta}^\dagger\overline{\Theta}|0_R\rangle$ and find the expression

$$\mathcal{I}(\sigma) = \langle 0_L|\overline{\Theta}^\dagger\overline{\Theta}|0_R\rangle x_{00}(\sigma), \quad (30)$$

for the Stieltjes integral transform. Here

$$x_{00}(\sigma) = \mathbf{w}_0\left[\mathbf{M}(\sigma)\right]^{-1}\mathbf{v}_0. \quad (31)$$

From the identity $\mathbb{I} = \mathbf{M}(\sigma)[\mathbf{M}(\sigma)]^{-1}$, one finds the linear system

$$\sum_\beta M_{\alpha\beta}(\sigma)x_{\beta 0}(\sigma) = \delta_{\alpha 0}, \quad (32)$$

where we defined $x_{\beta 0}(\sigma) = [\mathbf{M}(\sigma)^{-1}]_{\beta 0}$. Using Cramer's rule to solve the linear system, we find that $x_{00}(\sigma)$ is given by the continued fraction

$$x_{00}(\sigma) = \cfrac{1}{(a_0-\sigma) - \cfrac{b_0^2}{(a_1-\sigma) - \cfrac{b_1^2}{(a_2-\sigma)-\cdots}}}, \quad (33)$$

and finally Eq. (30) becomes

$$\mathcal{I}(\sigma) = \langle 0_L|\overline{\Theta}^\dagger\overline{\Theta}|0_R\rangle \left\{ \cfrac{1}{(a_0-\sigma) - \cfrac{b_0^2}{(a_1-\sigma) - \cfrac{b_1^2}{(a_2-\sigma)-\cdots}}} \right\}. \quad (34)$$

Then, from Eq. (9), one finds that the electric dipole polarizability is the continued fraction

$$\alpha_D = 2\alpha\langle 0_L|\overline{\Theta}^\dagger\overline{\Theta}|0_R\rangle \lim_{\sigma\to 0^+}\left\{\frac{1}{(a_0+\sigma)-\frac{b_0^2}{(a_1+\sigma)-\frac{b_1^2}{(a_2+\sigma)-\cdots}}}\right\}, \tag{35}$$

which is equivalent to the Lanczos sum rule of Ref. [28]. We note that Eq. (35) is an exact result if the operators $\hat{T}$ and $\hat{\mathcal{R}}$ are expanded up to Ap-Ah excitations in a nucleus with mass number A. However, in practical calculations $\hat{T}$ and $\hat{\mathcal{R}}$ are truncated since a full expansion is not feasible due to the very high computational cost. In this paper we truncate $\hat{T}$ and $\hat{\mathcal{R}}$ at singles-and-doubles excitations. However, we remind the reader that such a truncation includes exponentiated 1p-1h and 2p-2h excitations. The exponent yields also products of higher order. As the GDR consists of a superposition of 1p-1h excitations, a truncation at singles-and-doubles only is expected to be a good approximation. Similarly, the dipole polarizability is most sensitive to the GDR. The CCSD truncation has been shown to agree with the hyperspherical harmonics method within 1% for the radius and dipole polarizability of ^{4}He [34]. The effect of neglected 3p-3h excitations on these observables in heavier nuclei will be investigated in future work.

Summarizing, we presented three different methods to evaluate the electric dipole polarizability: (i) compute the LIT for the dipole response, obtain $R(\omega)$ from its inversion – with inversions performed as described in Ref. [34, 48, 49] – and compute the dipole polarizability from Eq. (1); (ii) use Eq. (16) for $\Gamma \to 0$. (iii) use the continued fraction as in Eq. (35). The second method is in principle a discretization of the continuum and it will be interesting to compare it with the other two methods.

III. RESULTS

In Ref. [34, 35] coupled-cluster results for the dipole response in ^{4}He were benchmarked against virtually exact results from the effective interaction hyperspherical harmonics [50, 51] method. Those calculations were based on NN forces [52] from chiral EFT. In this paper we augment the Hamiltonians to include 3NFs from chiral EFT.

First, we check the convergence of our results with respect to model-space parameters and compare the three different calculational approaches for the dipole polarizability using the NNLO$_{\rm sat}$ interaction [26]. Then, we compare to experimental data for ^{4}He, ^{16}O and ^{22}O. We remark that the LIT inversions shown in this sections are obtained with a regularized least square fit technique and that bands may only be an under-estimation of the full error. Other procedures of inversion will be investigated in the future. Finally, we explore correlations of the dipole polarizability with the charge radius in ^{16}O and ^{40}Ca by employing a variety of Hamiltonians. In addition to NNLO$_{\rm sat}$ and the family of interactions from Ref. [53], we also use a large set of realistic NN potentials [52, 54–57] to probe systematic uncertainties in the underlying Hamiltonians.

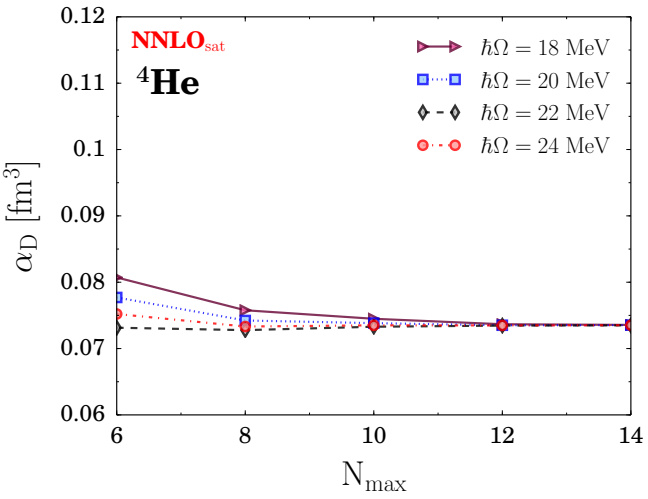

FIG. 2. (Color online) The electric dipole polarizability in ^{4}He as a function of the model space size $N_{\rm max}$. Curves for different values of $\hbar\Omega$, the underlying harmonic oscillator frequency, are shown.

When adding 3NFs, we use a Hartree-Fock basis built on 15 major harmonic oscillator shells. We vary the model space size up to $N_{\rm max}$ = 14 and we truncate the 3NFs matrix elements at $E_{3\rm max}$ = $N_{\rm max}$ for ^{4}He and ^{16,22}O. For our purposes, this truncation provides well-enough converged results. In fact, for the more challenging neutron-rich ^{22}O nucleus, increasing $E_{3\rm max}$ to 16 leads to a variation in energy of only 400 keV. For the calculations in ^{40}Ca with the NNLO$_{\rm sat}$ interaction and the Hamiltonians from Ref. [53] we employed the same $N_{\rm max}$ and $E_{3\rm max}$ truncations used for ^{48}Ca by Hagen *et al.* in Ref. [7].

A. The ^{4}He nucleus

Figure 2 shows the electric dipole polarizability of ^{4}He obtained from the continued fraction of Eq.(35) with the NNLO$_{\rm sat}$ interaction, as a function of the model space size $N_{\rm max}$. The four curves represent calculations with different values of oscillator frequency $\hbar\Omega$. The convergence in $N_{\rm max}$ is excellent and independence on $\hbar\Omega$ is reached with $N_{\rm max}$ = 14. The uncertainty at $N_{\rm max}$ = 14 for the different values of $\hbar\Omega$ is about 0.1%.

Let us compare the three different ways to calculate the dipole polarizability for ^{4}He as described at the end of Section II A. Equations (1) and (16) require an integration in energy and we present $\alpha_D(\varepsilon)$ where ε is the upper limit of the integration. Figure 3 shows the results. The blue band shows method (i), i.e. α_D is obtained from integrating Eq. (1), and $R(\omega)$ stems from an inversion of

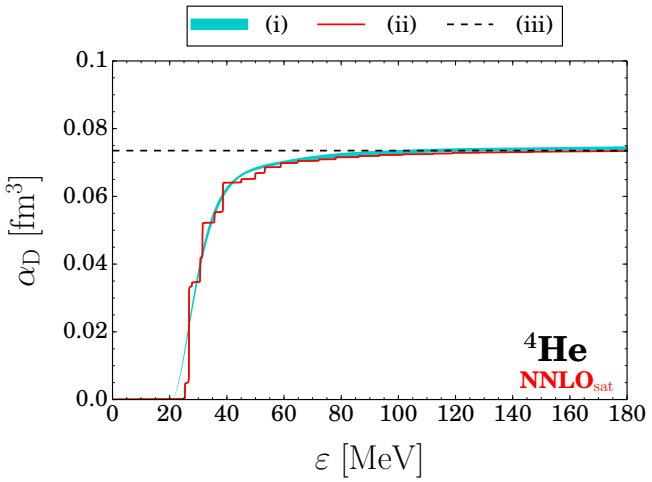

FIG. 3. (Color online) The electric dipole polarizability $\alpha_D(\varepsilon)$ in ^{4}He as a function of the integration energy ε: (i) using the LIT and Eq. (1) in blue (band); (ii) using Eq. (16) in red (solid); (iii) using the continued fraction of Eq. (35) in black (dashed). Calculations are performed for $\hbar\Omega$ = 22 MeV and $N_{\max}$ = 14.

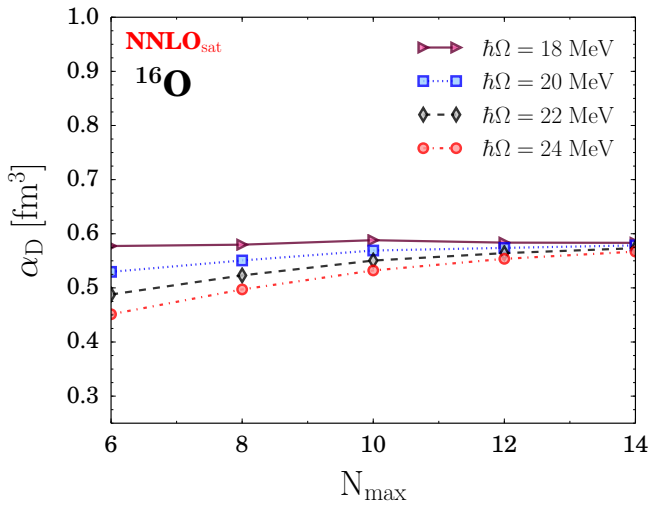

FIG. 4. (Color online) Electric dipole polarizability in ^{16}O as a function of the model space size $N_{\max}$ for different values of $\hbar\Omega$.

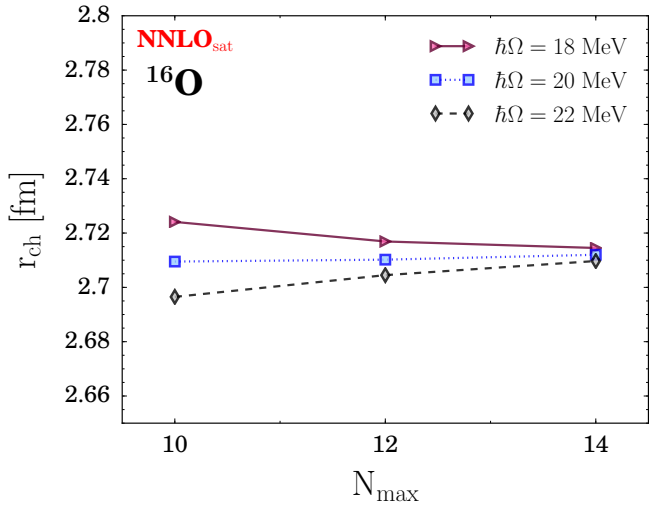

FIG. 5. (Color online) Charge radius in ^{16}O as a function of the model space size $N_{\max}$ for different values of $\hbar\Omega$.

the LIT. Here, the width of the blue band is an estimate of the uncertainty involved in the inversion procedure. The red solid line shows method (ii), i.e. α_D obtained from the LIT at small Γ using Eq. (16). The black dashed line shows the method (iii), i.e. α_D obtained using the continued fraction in Eq. (35).

We note that the different methods yield the same dipole polarizability. The integration methods (i) and (ii) exhibit a similar dependence on the integration range, the difference being that the former is smooth while the latter increases in steps. Here, method (ii) has the advantage of a sharper defined threshold. We also note that the dependence on the integration range is useful for comparisons with data for experiments that probe only a limited region of the energy spectrum.

B. The ^{16}O nucleus

Figure 4 shows the electric dipole polarizability in ^{16}O as a function of the model space size calculated with the NNLO$_{sat}$ interaction, while Figure 5 shows the same for the charge radius, which has been obtained from the point-proton radius taking into account contributions from nucleonic charge radii (see Ref. [7] for details). We observe that the curves for different $\hbar\Omega$ values converge very nicely and only a small residual $\hbar\Omega$-dependence remains at the largest model space size $N_{\max}$ = 14. Based on the spread of the different $\hbar\Omega$ curves for $N_{\max}$ = 14, we obtain a conservative error of 2.8% for the electric dipole polarizability and a conservative error of 0.7% for the charge radius.

Figure 6 compares the results from the three methods to obtain the polarizability for ^{16}O. The blue band (i) shows the integration as in Eq. (1) of the weighted response function, and the width of the band takes into account the uncertainty of the inversion. The red solid line (ii) refers to the integration of the weighted LIT with Eq. (16). The black dashed line (iii) is the reference value calculated with the continued fraction using Eq. (35). Again, we find good agreement of the results for the dipole polarizability.

C. The ^{22}O nucleus

The dipole strength of the neutron-rich nucleus ^{22}O was measured by Leistenschneider *et al.* [18] via Coulomb

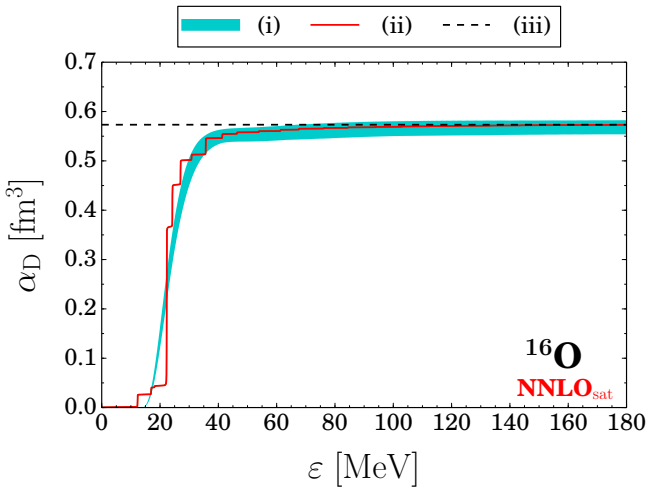

FIG. 6. (Color online) The electric dipole polarizability $\alpha_D(\varepsilon)$ in ^{16}O as a function of the integration limit ε. The blue band (i) is obtained integrating the weighted response function as in Eq. (1); the red solid curve (ii) is calculated integrating the weighted LIT at small Γ as in Eq. (16); the black dashed line (iii) is obtained from the continued fraction of Eq. (35). Calculations are performed with $N_{\max} = 14$ and $\hbar\Omega = 22$ MeV.

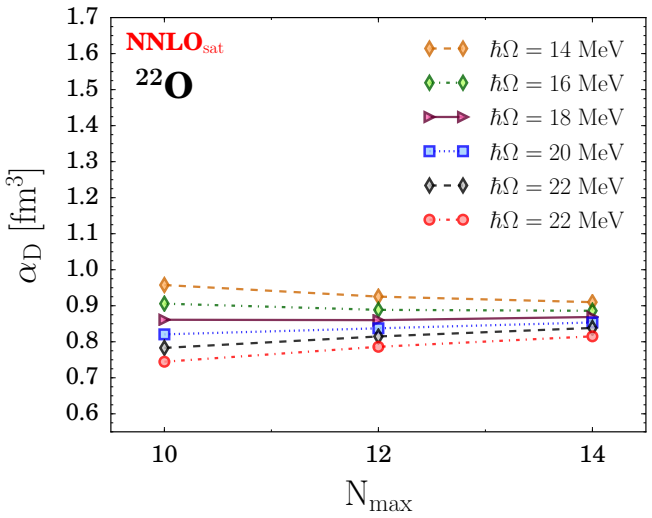

FIG. 7. (Color online) The electric dipole polarizability α_D in ^{22}O as a function of the model space size $N_{\max}$. Different curves for different values of the underlying harmonic oscillator basis frequency $\hbar\Omega$ are shown.

excitation in experiments at GSI. Figure 7 shows the electric dipole polarizability as a function of the model space size of the calculation. After having investigated various frequencies, we find that $\hbar\Omega = 18$ MeV is the best converging curve. However, the convergence for different $\hbar\Omega$ is slower than what observed in lighter nuclei, resulting in a conservative uncertainty of about 8% at $N_{\max} = 14$. This might be because the excess neutrons in ^{22}O are loosely bound, making the wave function more extended and thus the convergence slower. We note that α_D of ^{22}O is larger than for ^{16}O.

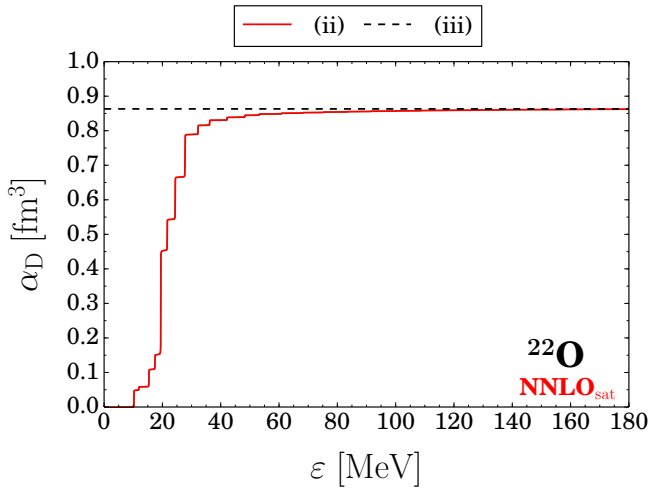

FIG. 8. (Color online) The electric dipole polarizability $\alpha_D(\varepsilon)$ in ^{22}O as a function of the integration limit ε. The red solid curve (ii) is calculated integrating the weighted LIT at small Γ as in Eq. (16); the black dashed line (iii) is obtained from the continued fraction of Eq. (35). Calculations are performed with $N_{\max} = 14$ and $\hbar\Omega = 18$ MeV.

Finally, in Figure 8 we show a comparison between the methods (ii) and (iii) to calculate α_D. We used the largest model space and the fastest converging frequency of $\hbar\Omega = 18$ MeV and find good agreement between the two methods. Because the convergence of the LIT calculations is not at sub-percent level, we cannot presently obtain stable inversions and include the method (i) in the comparison. Nevertheless, by looking at the laddered curve we learn about the convergence of this sum rule as a function of the energy. This will be used in the following Subsection to make a comparison with the experimental data from Ref. [18].

D. Comparison to experiment

Table I compares theoretical results with experimental data. We observe that for both ^{4}He and ^{16}O calculations are in good agreement with the experimental data. For ^{4}He the experimental data is obtained by combining measurements from Refs. [58–60]. We also present a comparison with other *ab initio* results obtained with hyperspherical harmonics [61, 62] and with the no-core shell model [63]. Because the experimental errorbar is quite large, all theoretical calculations are compatible with data.

For ^{16}O the calculation of the dipole polarizability with the NNLO$_{sat}$ interaction overlaps with the experimental value [64]. This is an improvement compared to the previous calculation limited to NN interaction only [65].

For the ^{22}O nucleus, to compare our calculations

TABLE I. Theoretical values of α_D for different nuclei calculated with the NNLO$_{\rm sat}$ interaction in comparison to experimental data from [58–60] and other calculations from Refs. [63] (a), [61] (b) and [62] (c) for ^{4}He, to experimental data from Ref. [64] for ^{16}O. For ^{22}O we compare to the value obtained integrating the data from Ref. [18] first over the whole energy range (d) and then only the first 3 MeV of the strength (e), corresponding to the low-lying dipole strength. Values are expressed in fm^3. The theoretical uncertainties of our calculations stem from the $\hbar\Omega$ dependence in the model space with $N_{\rm max}$ = 14.

Nucleus	Theory	Exp
^{4}He	0.0735(1)	0.074(9)
	0.0673(5)^a	
	0.0655^b	
	0.0651^c	
	0.0694^c	
^{16}O	0.57(1)	0.585(9)
^{22}O	0.86(4)	0.43(4)^d
	0.05(1)	0.07(2)^e

with experimental data we integrate the experimental strength of Ref. [18] up to the available energy range of about 18 MeV above threshold, obtaining α_D^{exp} = 0.43(4) fm^3. This value is much lower than our calculated α_D^{th} = 0.86(4) fm^3 shown in Figure 8, which corresponds to the integration of the strength up to infinity. The theoretical result exceeds the experimental value by a factor of two and we also find that the integration of the theoretical strength over the first 18 MeV exhausts the 87% of the polarizability sum rule. On the other hand, Leistenschneider *et al.* observed a PDR extending for about 3 MeV above the neutron emission threshold of S_n = 6.85 MeV. Integrating the data over this interval yields a dipole polarizability $\alpha_D^{\rm exp}$(3 MeV) = 0.07(2) fm^3. While our calculations in Figure 8 does not reproduce the experimental threshold, integration over the first 3 MeV of the strength and considering the different $\hbar\Omega$ frequencies yields α_D^{th}(PDR) = 0.05(1) fm^3. This is consistent with the experimental result.

In Figure 9 we show the response function of ^{4}He. The response function is obtained from the inversion of the LIT as described in Refs. [34, 48, 49] and the width of the band is an estimate of the inversion uncertainty. The dark band from Ref. [35] is the result obtained with coupled cluster with singles-and-doubles (CCSD) using a NN interaction at next-to-next-to-next-to-leading order (N3LO) [52]. The light band represents the calculation of this work with NNLO$_{\rm sat}$ [26] and it has been obtained by inverting the LIT with Γ = 10 and 20 MeV calculated at $N_{\rm max}$ = 14 and $\hbar\Omega$ = 22 MeV. This is also the curve that has been integrated with method (i) in Figure 3. To emphasize the shape of the response function in the continuum, in Figure 9 we shift the N3LO curve to the experimental threshold, *i.e.*, from 17.54 MeV (theory) to 19.8 MeV (experiment), while the NNLO$_{\rm sat}$ threshold well reproduces the experimental one since the potential is fitted to binding energies of ^{4}He and ^{3}H. We find that the NNLO$_{\rm sat}$ response function, which includes three-nucleon forces, presents a larger peak with respect to other results with three-nucleon forces from Refs. [66, 67]. Finally, the theoretical results are compared with the experimental data by Nakayama *et al.* [68] (blue circles), Arkatov *et al.* [58, 59] (white squares), Nilsson *et al.* [69] (yellow squares), Shima *et al.* [70, 71] (magenta circles) and Tornow *et al.* [72] (green squares).

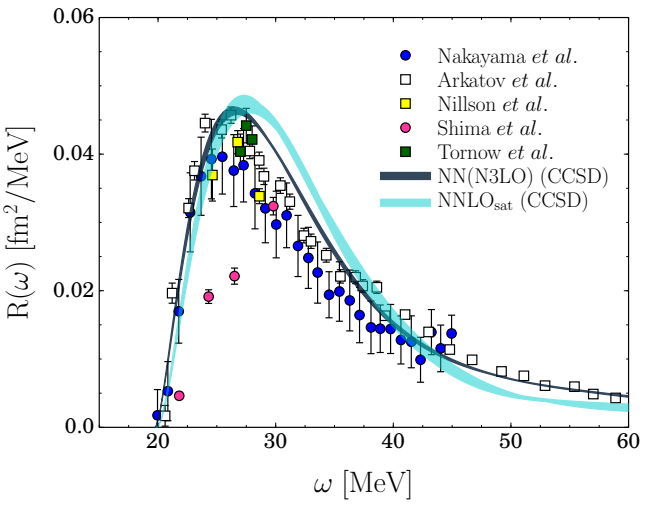

FIG. 9. (Color online) ^{4}He photo-absorption response function calculated with different methods and interactions (see text for details) compared with experimental data from by Nakayama *et al.* [68] (blue circles), Arkatov *et al.* [58, 59] (white squares), Nilsson *et al.* [69] (yellow squares), Shima *et al.* [70, 71] (magenta circles) and Tornow *et al.* [72] (green squares).

In Figure 10 we show the response function for ^{16}O calculated with a NN interaction using CCSD [35] (light band) and then with NNLO$_{\rm sat}$ (dark band). The calculations are compared with the experimental data from Ahrens *et al.* [64] (triangles with error bars) and Ishkhanov *et al.* [73] (red circles). The response function with NNLO$_{\rm sat}$ has been obtained again by inverting the LIT with both Γ = 10 and 20 MeV and at frequency $\hbar\Omega$ = 22 MeV. The large error band for the NNLO$_{\rm sat}$ results from the fact that the largest available model space size in our calculation, namely $N_{\rm max}$ = 14, is smaller than the $N_{\rm max}$ = 18 used for the N3LO potential. Similarly to what is done for ^{4}He, also in this case we plot the theoretical curves to start from the experimental threshold, *i.e.*, we shift the N3LO (NNLO$_{\rm sat}$) curve from their threshold of 14.25 (10.69 [26]) MeV to the experimental value of 12.1 MeV. In particular, for the NNLO$_{\rm sat}$, we have found that using the threshold energy as a fit parameter in the inversion, we obtain response functions that correctly reproduce α_D only with a threshold energy varied around

5% of the experimental value. Overall, it is interesting to see that three-nucleon forces enhance the strength, slightly improving the comparison with the experimental data.

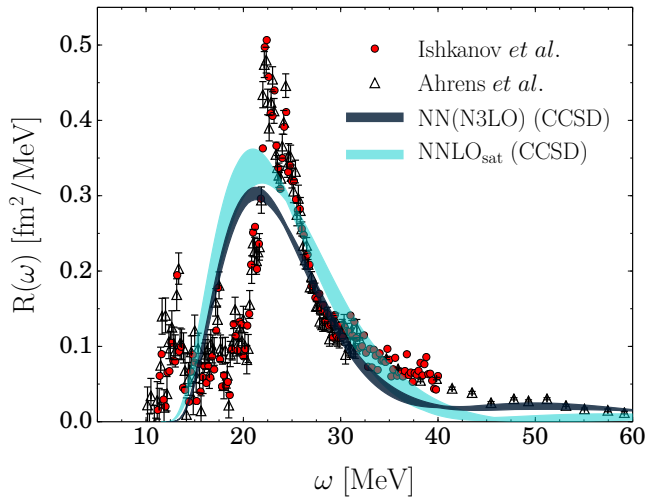

FIG. 10. (Color online) ^{16}O photo-absorption response function calculated with coupled cluster with singles-and-doubles using a NN interaction only [35, 52] (dark band) and NNLO$_{sat}$ [26] (Light band). The red circles are the experimental data from Ishkhanov *et al.* [73] while the white triangles with error bars are the experimental results by Ahrens *et al.* [64].

Comparing Figure 3 and 6 with Figure 9 and 10 respectively, and taking into account the results summarized in Table I, it is clear that the polarizability is not very sensitive to the structure and shape of the response function, but rather to the distribution of the dipole strength at low energies.

E. Correlations between α_D and r_{ch}

Let us also attempt to probe systematic theoretical uncertainties that are due to the employed interaction by considering results from different families of Hamiltonians. Such an approach can help to correlate observables of interest, see Refs. [4–7, 74–76] for examples. To study such correlations, one needs a considerable number of different interactions, so that one can obtain results spanning a wide range of values for the observables under investigation. For this reason, we choose to use similarity renormalization group (SRG) [55] and V$_{low-k}$ [56] evolutions as a tool to generate a set of phase-shift equivalent two-body interactions. When adding three nucleon forces at next-to-next-to-leading order – without considering the induced three-body forces – the low-energy constants were recalibrated on light nuclei observables [53]. Finally, we also consider the newly developed NNLO$_{sat}$ interaction [26], which well reproduces radii [7].

We note that a correlation between the electric dipole polarizability and the nuclear charge radius r_{ch} is expected from the nuclear droplet models [77, 78] in heavy nuclei. In what follows we investigate correlations between the dipole polarizability and charge radius in ^{16}O and ^{40}Ca using a variety of interactions. We base our calculations on NN forces and 3NFs from Refs. [26, 53], and also consider computations limited to NN forces alone. Results with 3NFs are also listed in Table II for ^{16}O and ^{40}Ca (some were previously published in Refs. [7, 26] while others have been newly calculated).

TABLE II. List of results with three-body Hamiltonians [26, 53] for ground-state energy per nucleon, charge radius and electric dipole polarizability, plotted in Fig. 11. For the notation of the potentials we follow Ref. [53]. Energies have been obtained with a Λ – CCSD(T) approximation [42, 79, 80]. Experimental values are taken from Ref. [81] (energy), Ref. [82] (radius) and Ref. [64] (electric dipole polarizability).

^{16}O			
Interaction	E_0/A [MeV]	$r_{\rm ch}$ [fm]	α_D [fm^3]
2.0.2.0(EM)	-7.70	2.62	0.46
2.2/2.0(PWA)	-7.14	2.74	0.54
1.8/2.0(EM)	-7.98	2.60	0.44
2.2/2.0(EM)	-7.50	2.63	0.48
2.8/2.0(EM)	-7.16	2.67	0.52
NNLO$_{sat}$	-7.68	2.71	0.58
Experiment	-7.98	2.6991(52)	0.58(1)
^{40}Ca			
2.0.2.0(EM)	-8.22	3.35	1.67
2.2/2.0(PWA)	-7.24	3.55	2.03
1.8/2.0(EM)	-8.69	3.31	1.57
2.2/2.0(EM)	-7.89	3.38	1.75
2.8/2.0(EM)	-7.35	3.44	1.94
NNLO$_{sat}$	-8.15	3.48	2.08
Experiment	-8.55	3.4776(19)	2.23(3)

Figure 11 shows α_D – calculated with method (iii) – as a function of r_{ch} in ^{16}O and ^{40}Ca for various interactions. The charge radii are based on the point-proton radii with contributions from nucleonic charge radii, see Ref. [7] for details. Empty symbols correspond to calculations with NN potentials only. In particular, (a) is obtained from SRG evolved Entem and Machleidt [52] interaction with cutoff Λ = 500 MeV and, in order of decreasing r_{ch} values, $\lambda = \infty, 3.5, 3.0, 2.5$ and 2.0 fm^{-1}, while for (b) we used the same interaction with cutoff Λ = 600 MeV and, in order of decreasing r_{ch} values, λ = 3.5, 3.0 and 2.5 fm^{-1}. The points (c) represented with triangles pointing up are calculations with the SRG evolved CD-BONN [54] potential with, in order of decreasing r_{ch} value, λ = 4.0 and 3.5 fm^{-1}, while the triangles pointing down (d) are calculations with the V$_{low-k}$ [56] evolved CD-BONN interaction and λ = 3.0, 2.5 and 2.0 fm^{-1}. The hexagons (e) are calculations with V$_{low-k}$-evolved AV18 [57] interaction and λ = 3.0 and 2.5 fm^{-1}, in order of decreasing radius. The red diamonds (f) are calculations including 3NFs. The larger red diamond is the value obtained with NNLO$_{sat}$ [26], while the smaller ones are the potentials from Ref. [53] also used for the calculations in ^{48}Ca in

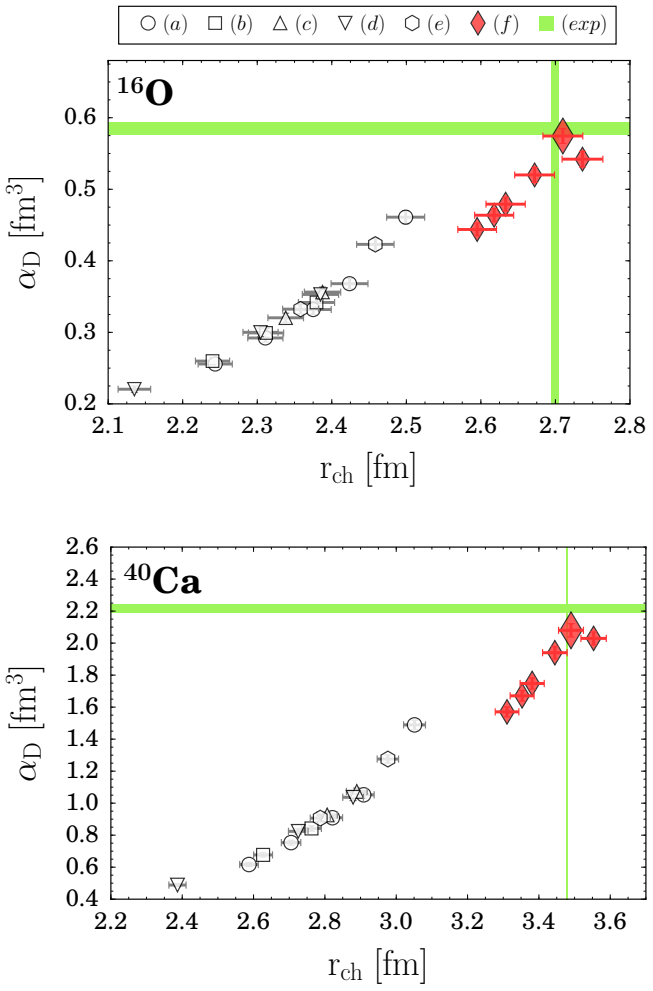

FIG. 11. (Color online) α_D versus r_{ch} in ^{16}O and ^{40}Ca. Empty symbols refer to calculations with NN potentials only: (a) SRG evolved Entem-Machleidt interaction [52] with Λ = 500 MeV/c and $\lambda = \infty, 3.5, 3.0, 2.5$ and 2.0 fm^{-1}, (b) SRG evolved Entem-Machleidt interaction [52] with Λ = 600 MeV/c and λ = 3.5, 3.0 and 2.5 fm^{-1}, (c) SRG evolved CD-BONN [54] interaction with λ = 4.0 and 3.5 fm^{-1}, (d) V$_{low-k}$ evolved CD-BONN potentials with λ = 3.0, 2.5 and 2.0 fm^{-1} and (e) V$_{low-k}$-evolved AV18 [57] interaction and λ = 3.0 and 2.5 fm^{-1}. The red diamonds (f) refer to calculations that include 3NF: the large one is from NNLO$_{\rm sat}$ [26] and the others from chiral interactions as in Ref. [53]. The green bands (exp), show the experimental data [64, 82].

Ref. [7]. The error bars for the calculations represent uncertainties arising both from the coupled-cluster truncation scheme and the model space truncations and are estimated to be of the order of 1% for the charge radius and 2% for the polarizability (see Ref. [7] for details). Finally, the green bands are the experimental values for the polarizability [64] and the charge radius [82], respectively.

We note that α_D and r_{ch} are strongly correlated. We also note that NN interactions alone systematically underestimate both α_D and r_{ch} while the inclusion of 3NFs improves the agreement with data. The agreement with data is particularly good for the interaction NNLO$_{\rm sat}$. We note that one cannot blindly use a correlation between theoretical data points to extrapolate to experimental results. The data based on NN interactions, even when extrapolated with a simple linear or quadratic curve, does not meet the experimental values. In contrast, the results from NN and 3NFs can be interpolated (when e.g. the charge radius is known) to yield a sensible prediction for the dipole polarizability.

IV. CONCLUSIONS

In conclusion, we employed integral transforms to compute the electric dipole polarizability in beta-stable nuclei and rare isotopes. This approach employs bound-state technology but takes the continuum properly into account. We presented in detail the formalism for coupled-cluster calculations of α_D and computed the dipole polarizability in ^{4}He, ^{16,22}O, and ^{40}Ca. Formulations as the dipole polarizability as an energy-weighted sum rule facilitate the comparison to data in cases where only lower-lying dipole strengths are measured.

The comparison with data reveals the important role of three-nucleon forces, and results based on the NNLO$_{\rm sat}$ interaction agree well with data in ^{4}He and ^{16}O, and ^{40}Ca. For the neutron-rich ^{22}O, the low-lying dipole strength within 3 MeV of threshold theoretical results are consistent with data, while the total theoretical dipole strength is about a factor of two larger than what can be computed from the available data. Further investigation is needed to study the shape of the low-energy strength distribution.

Finally, we studied ^{16}O and ^{40}Ca with different two- and three-body interactions and observed a strong correlation between the dipole polarizability and the charge radius. Such a correlation could be useful to predict either of the two observables, when only one of them is experimentally known. Work in this direction is underway for heavier nuclei, such as ^{68}Ni and ^{90}Zr.

ACKNOWLEDGMENTS

TRIUMF receives federal funding via a contribution agreement with the National Research Council of Canada. This work was supported in parts by the Natural Sciences and Engineering Research Council (Grant number SAPIN-2015-00031), the US-Israel Binational Science Foundation (Grant No. 2012212), the Pazy Foundation, the MIUR grant PRIN-2009TWL3MX, the Office of Nuclear Physics, U.S. Department of Energy under Grants Nos. DE-FG02-96ER40963 (University of Tennessee) and DE-SC0008499 (NUCLEI SciDAC collaboration), and the Field Work Proposal ERKBP57 at Oak Ridge National Laboratory. Computer time was provided by the Innovative and Novel Computational Impact

on Theory and Experiment (INCITE) program. This research used resources of the Oak Ridge Leadership Computing Facility located in the Oak Ridge National Laboratory, supported by the Office of Science of the U.S. Department of Energy under Contract No. DE-AC05-00OR22725, and computational resources of the National Center for Computational Sciences, the National Institute for Computational Sciences, and TRIUMF.

[1] B. L. Berman and S. C. Fultz, Rev. Mod. Phys. **47**, 713–761 (1975).
[2] T. Kobayashi, S. Shimoura, I. Tanihata, K. Katori, K. Matsuta, T. Minamisono, K. Sugimoto, W. Müller, D. L. Olson, T. J. M. Symons, and H. Wieman, Phys. Lett. B **232**, 51 – 55 (1989).
[3] T. Aumann and T. Nakamura, Physica Scripta **2013**, 014012 (2013).
[4] P.-G. Reinhard and W. Nazarewicz, Phys. Rev. C **81**, 051303 (2010).
[5] J. Piekarewicz, B. K. Agrawal, G. Colò, W. Nazarewicz, N. Paar, P.-G. Reinhard, X. Roca-Maza, and D. Vretenar, Phys. Rev. C **85**, 041302 (2012).
[6] X. Roca-Maza, X. Viñas, M. Centelles, B. K. Agrawal, G. Colò, N. Paar, J. Piekarewicz, and D. Vretenar, Phys. Rev. C **92**, 064304 (2015).
[7] G. Hagen, A. Ekström, G. R. Jansen, W. Nazarewicz, T. Papenbrock, K. A. Wendt, B. Carlsson, C. Forssén, M. Hjorth-Jensen, S. Bacca, N. Barnea, M. Miorelli, G. Orlandini, C. Drischler, K. Hebeler, A. Schwenk, and J. Simonis, Nature Physics **12**, 186–190 (2016).
[8] B. A. Brown, Phys. Rev. Lett. **85**, 5296–5299 (2000).
[9] R. J. Furnstahl, Nucl. Phys. A **706**, 85 – 110 (2002).
[10] M. B. Tsang, J. R. Stone, F. Camera, P. Danielewicz, S. Gandolfi, K. Hebeler, C. J. Horowitz, Jenny Lee, W. G. Lynch, Z. Kohley, R. Lemmon, P. Möller, T. Murakami, S. Riordan, X. Roca-Maza, F. Sammarruca, A. W. Steiner, I. Vidaña, and S. J. Yennello, Phys. Rev. C **86**, 015803 (2012).
[11] K. Hebeler and A. Schwenk, The European Physical Journal A **50**, 1–7 (2014).
[12] L. Trippa, G. Colò, and E. Vigezzi, Phys. Rev. C **77**, 061304 (2008).
[13] A. Carbone, G. Colò, A. Bracco, L.-G. Cao, P. F. Bortignon, F. Camera, and O. Wieland, Phys. Rev. C **81**, 041301 (2010).
[14] A. Tamii, I. Poltoratska, P. von Neumann-Cosel, Y. Fujita, T. Adachi, C. A. Bertulani, J. Carter, M. Dozono, H. Fujita, K. Fujita, K. Hatanaka, D. Ishikawa, M. Itoh, T. Kawabata, Y. Kalmykov, A. M. Krumbholz, E. Litvinova, H. Matsubara, K. Nakanishi, R. Neveling, H. Okamura, H. J. Ong, B. Özel-Tashenov, V. Yu. Ponomarev, A. Richter, B. Rubio, H. Sakaguchi, Y. Sakemi, Y. Sasamoto, Y. Shimbara, Y. Shimizu, F. D. Smit, T. Suzuki, Y. Tameshige, J. Wambach, R. Yamada, M. Yosoi, and J. Zenihiro, Phys. Rev. Lett. **107**, 062502 (2011).
[15] D. M. Rossi, P. Adrich, F. Aksouh, H. Alvarez-Pol, T. Aumann, J. Benlliure, M. Böhmer, K. Boretzky, E. Casarejos, M. Chartier, A. Chatillon, D. Cortina-Gil, U. Datta Pramanik, H. Emling, O. Ershova, B. Fernandez-Dominguez, H. Geissel, M. Gorska, M. Heil, H. T. Johansson, A. Junghans, A. Kelic-Heil, O. Kiselev, A. Klimkiewicz, J. V. Kratz, R. Krücken, N. Kurz, M. Labiche, T. Le Bleis, R. Lemmon, Yu. A. Litvinov, K. Mahata, P. Maierbeck, A. Movsesyan, T. Nilsson, C. Nociforo, R. Palit, S. Paschalis, R. Plag, R. Reifarth, D. Savran, H. Scheit, H. Simon, K. Sümmerer, A. Wagner, W. Waluś, H. Weick, and M. Winkler, Phys. Rev. Lett. **111**, 242503 (2013).
[16] A. M. Krumbholz, P. von Neumann-Cosel, T. Hashimoto, A. Tamii, T. Adachi, C. A. Bertulani, H. Fujita, Y. Fujita, E. Ganioglu, K. Hatanaka, C. Iwamoto, T. Kawabata, N. T. Khai, A. Krugmann, D. Martin, H. Matsubara, R. Neveling, H. Okamura, H. J. Ong, I. Poltoratska, V. Yu. Ponomarev, A. Richter, H. Sakaguchi, Y. Shimbara, Y. Shimizu, J. Simonis, F. D. Smit, G. Susoy, J. H. Thies, T. Suzuki, M. Yosoi, and J. Zenihiro, Phys. Lett. B **744**, 7 – 12 (2015).
[17] T. Hashimoto, A. M. Krumbholz, P.-G. Reinhard, A. Tamii, P. von Neumann-Cosel, T. Adachi, N. Aoi, C. A. Bertulani, H. Fujita, Y. Fujita, E. Ganioğlu, K. Hatanaka, E. Ideguchi, C. Iwamoto, T. Kawabata, N. T. Khai, A. Krugmann, D. Martin, H. Matsubara, K. Miki, R. Neveling, H. Okamura, H. J. Ong, I. Poltoratska, V. Yu. Ponomarev, A. Richter, H. Sakaguchi, Y. Shimbara, Y. Shimizu, J. Simonis, F. D. Smit, G. Süsoy, T. Suzuki, J. H. Thies, M. Yosoi, and J. Zenihiro, Phys. Rev. C **92**, 031305 (2015).
[18] A. Leistenschneider, T. Aumann, K. Boretzky, D. Cortina, J. Cub, U. Datta Pramanik, W. Dostal, Th. W. Elze, H. Emling, H. Geissel, A. Grünschloß, M. Hellstr, R. Holzmann, S. Ilievski, N. Iwasa, M. Kaspar, A. Kleinböhl, J. V. Kratz, R. Kulessa, Y. Leifels, E. Lubkiewicz, G. Münzenberg, P. Reiter, M. Rejmund, C. Scheidenberger, C. Schlegel, H. Simon, J. Stroth, K. Sümmerer, E. Wajda, W. Walús, and S. Wan, Phys. Rev. Lett. **86**, 5442–5445 (2001).
[19] S. Bacca and S. Pastore, J. Phys. **G41**, 123002 (2014).
[20] R. Roth, A. Calci, J. Langhammer, and S. Binder, Few-Body Systems **55**, 659–665 (2014).
[21] S. Quaglioni, G. Hupin, A. Calci, P. Navrátil, and R. Roth, European Physical Journal Web of Conferences **113**, 01005 (2016).
[22] B. D. Carlsson, A. Ekström, C. Forssén, D. F. Strömberg, G. R. Jansen, O. Lilja, M. Lindby, B. A. Mattsson, and K. A. Wendt, Phys. Rev. X **6**, 011019 (2016).
[23] S. Wesolowski, N. Klco, R. J. Furnstahl, D. R. Phillips, and A. Thapaliya, (2015), arXiv:1511.03618 [nucl-th].
[24] R. J. Furnstahl, D. R. Phillips, and S. Wesolowski, J. Phys. G **42**, 034028 (2015).
[25] S. Binder, A. Calci, E. Epelbaum, R. J. Furnstahl, J. Golak, K. Hebeler, H. Kamada, H. Krebs, J. Langhammer, S. Liebig, P. Maris, U.-G. Meißner, D. Minossi, A. Nogga, H. Potter, R. Roth, R. Skibinski, K. Topolnicki, J. P. Vary, and H. Witala, (2015), arXiv:1505.07218 [nucl-th].
[26] A. Ekström, G. R. Jansen, K. A. Wendt, G. Hagen,

T. Papenbrock, B. D. Carlsson, C. Forssén, M. Hjorth-Jensen, P. Navrátil, and W. Nazarewicz, Phys. Rev. C **91**, 051301 (2015).
[27] For simplicity, in this notation we omit the average on projections of the initial angular momentum.
[28] N. Nevo Dinur, N. Barnea, C. Ji, and S. Bacca, Phys. Rev. C **89**, 064317 (2014).
[29] V.D. Efros, Sov. J. Nucl. Phys. **41**, 949 (1985).
[30] V. D. Efros, W. Leidemann, and G. Orlandini, Physics Letters B **338**, 130 – 133 (1994).
[31] V. D. Efros, W. Leidemann, Orlandini.G., and N. Barnea, J. Phys. G **34**, R459 (2007).
[32] V.D. Efros, W. Leidemann, and G. Orlandini, Few-Body Systems **14**, 151–170 (1993).
[33] A.-I N. Tikhonov, *Solutions of ill posed problems*, Scripta series in mathematics (Vh Winston, 1977).
[34] S. Bacca, N. Barnea, G. Hagen, G. Orlandini, and T. Papenbrock, Phys. Rev. Lett. **111**, 122502 (2013).
[35] S. Bacca, N. Barnea, G. Hagen, M. Miorelli, G. Orlandini, and T. Papenbrock, Phys. Rev. C **90**, 064619 (2014).
[36] F. Coester, Nucl. Phys. **7**, 421 – 424 (1958).
[37] F. Coester and H. Kümmel, Nucl. Phys. **17**, 477 – 485 (1960).
[38] H. Kümmel, K. H. Lührmann, and J. G. Zabolitzky, Physics Reports **36**, 1 – 63 (1978).
[39] B. Mihaila and J. H. Heisenberg, Phys. Rev. Lett. **84**, 1403–1406 (2000).
[40] D. J. Dean and M. Hjorth-Jensen, Phys. Rev. C **69**, 054320 (2004).
[41] M. Włoch, D. J. Dean, J. R. Gour, M. Hjorth-Jensen, K. Kowalski, T. Papenbrock, and P. Piecuch, Phys. Rev. Lett. **94**, 212501 (2005).
[42] G. Hagen, T. Papenbrock, D. J. Dean, and M. Hjorth-Jensen, Phys. Rev. C **82**, 034330 (2010).
[43] S. Binder, J. Langhammer, A. Calci, and R. Roth, Phys. Lett. B **736**, 119 – 123 (2014).
[44] R. J. Bartlett and M. Musiał, Rev. Mod. Phys. **79**, 291–352 (2007).
[45] G. Hagen, T. Papenbrock, M. Hjorth-Jensen, and D. J. Dean, Rep. Prog. Phys. **77**, 096302 (2014).
[46] J. F. Stanton and R. J. Bartlett, J. Chem. Phys. **98**, 7029–7039 (1993).
[47] J. K. Cullum, Technical Report **CS-TR-3576** (1998).
[48] D. Andreasi, W. Leidemann, C. Rei, and M. Schwamb, The European Physical Journal A - Hadrons and Nuclei **24**, 361–372 (2005).
[49] V. D. Efros, W. Leidemann, and G. Orlandini, Few-Body Systems **26**, 251–269 (1999).
[50] N. Barnea, W. Leidemann, and G. Orlandini, Phys. Rev. C **61**, 054001 (2000).
[51] R. Goerke, S. Bacca, and N. Barnea, Phys. Rev. C **86**, 064316 (2012).
[52] D. R. Entem and R. Machleidt, Phys. Rev. C **68**, 041001 (2003).
[53] K. Hebeler, S. K. Bogner, R. J. Furnstahl, A. Nogga, and A. Schwenk, Phys. Rev. C **83**, 031301 (2011).
[54] R. Machleidt, Phys. Rev. C **63**, 024001 (2001).
[55] S. K. Bogner, R. J. Furnstahl, and R. J. Perry, Phys. Rev. C **75**, 061001 (2007).
[56] S. K. Bogner, T. T. S. Kuo, and A. Schwenk, Phys. Rep. **386**, 1 – 27 (2003).
[57] R. B. Wiringa, V. G. J. Stoks, and R. Schiavilla, Phys. Rev. C **51**, 38 (1995).
[58] Yu. M. Arkatov, P. I. Vatset, V. I. Voloshuchuk, V. A. Zolenko, I. M. Prokhorets, and V. I. Chimil, Sov. J. Nucl. Phys. **19**, 598 (1974).
[59] Yu. M. Arkatov, P. I. Vatset, V. I. Voloshuchuk, V. A. Zolenko, and I. M. Prokhorets, Sov. J. Nucl. Phys. **31**, 726 (1980).
[60] K. Pachucki and A. M. Moro, Phys. Rev. A **75**, 032521 (2007).
[61] D. Gazit, N. Barnea, S. Bacca, W. Leidemann, and G. Orlandini, Phys. Rev. C **74**, 061001 (2006).
[62] C. Ji, N. Nevo Dinur, S. Bacca, and N. Barnea, Phys. Rev. Lett. **111**, 143402 (2013).
[63] I. Stetcu, S. Quaglioni, J. L. Friar, A. C. Hayes, and Petr Navrátil, Phys. Rev. C **79**, 064001 (2009).
[64] J. Ahrens, H. Borchert, K.H. Czock, H.B. Eppler, H. Gimm, H. Gundrum, M. Kröning, P. Riehn, G. Sita Ram, A. Zieger, and B. Ziegler, Nuclear Physics A **251**, 479 – 492 (1975).
[65] M. Miorelli, S. Bacca, N. Barnea, G. Hagen, G. Orlandini, and T. Papenbrock, EPJ Web of Conferences **113**, 04007 (2016).
[66] D. Gazit, S. Bacca, N. Barnea, W. Leidemann, and G. Orlandini, Phys. Rev. Lett. **96**, 112301 (2006).
[67] S. Quaglioni and P. Navrátil, Physics Letters B **652**, 370 – 375 (2007).
[68] S. Nakayama, E. Matsumoto, R. Hayami, K. Fushimi, H. Kawasuso, K. Yasuda, T. Yamagata, H. Akimune, H. Ikemizu, M. Fujiwara, M. Yosoi, K. Nakanishi, K. Kawase, H. Hashimoto, T. Oota, K. Sagara, T. Kudoh, S. Asaji, T. Ishida, M. Tanaka, and M. B. Greenfield, Phys. Rev. C **76**, 021305 (2007).
[69] B. Nilsson, J.-O. Adler, B.-E. Andersson, J.R.M. Annand, I. Akkurt, M.J. Boland, G.I. Crawford, K.G. Fissum, K. Hansen, P.D. Harty, D.G. Ireland, L. Isaksson, M. Karlsson, M. Lundin, J.C. McGeorge, G.J. Miller, H. Ruijter, A. Sandell, B. Schrder, D.A. Sims, and D. Watts, Physics Letters B **626**, 65 – 71 (2005).
[70] T. Shima, S. Naito, Y. Nagai, T. Baba, K. Tamura, T. Takahashi, T. Kii, H. Ohgaki, and H. Toyokawa, Phys. Rev. C **72**, 044004 (2005).
[71] T. Shima, Y. Nagai, S. Miyamoto, S. Amano, K. Horikawa, T. Mochizuki, H. Utsunomiya, and H. Akimune, AIP Conference Proceedings **1235**, 315–321 (2010).
[72] W. Tornow, J. H. Kelley, R. Raut, G. Rusev, A. P. Tonchev, M. W. Ahmed, A. S. Crowell, and S. C. Stave, Phys. Rev. C **85**, 061001 (2012).
[73] B. S. Ishkhanov, I. M. Kapitonov, E. I. Lileeva, E. V. Shirokov, V. A. Erokhova, M. A. Elkin, and A. V. Izotova, Tech. Rep. MSU-INP-2002-27/711 (Institute of Nuclear Physics, Moscow State University, 2002).
[74] A. Nogga, S. K. Bogner, and A. Schwenk, Phys. Rev. C **70**, 061002 (2004).
[75] L. Platter, H.-W. Hammer, and U.-G. Meißner, Phys. Lett. B **607**, 254 – 258 (2005).
[76] A. Calci and R. Roth, Phys. Rev. C **94**, 014322 (2016).
[77] W. D. Myers, W. J. Swiatecki, T. Kodama, L. J. El-Jaick, and E. R. Hilf, Phys. Rev. C **15**, 2032–2043 (1977).
[78] E. Lipparini and S. Stringari, Phys. Rep. **175**, 104 (1989).
[79] A. G. Taube and R. J. Bartlett, The Journal of Chemical Physics **128**, 044110 (2008).
[80] S. Binder, P. Piecuch, A. Calci, J. Langhammer, P. Navrátil, and R. Roth, Phys. Rev. C **88**, 054319 (2013).

[81] BNL, "National nuclear data center," (2016).

[82] I. Angeli and K.P. Marinova, Atomic Data and Nuclear Data Tables **99**, 69 – 95 (2013).